Available online at www.sciencedirect.com
SCIENCE DIRECT®
NDT&E International 36 (2003) 587–599
NDT&E international
www.elsevier.com/locate/ndteint

Explicit geometric model of a radioscopic imaging system

Domingo Mery*,[1]

Departamento de Ingeniería Informática, Facultad de Ingenieria, Universidad de Santiago de Chile, Av. Ecuador 3659, P.O. Box 7251657, Santiago, Chile

Received 15 September 2002; revised 28 April 2003; accepted 2 June 2003

Abstract

In this paper a new explicit model of a radioscopic imaging system is presented. The model includes three parts: X-ray projection, image intensifier and CCD camera. The X-ray projection is modelled as a linear central projection. The image intensifier is modelled using a new explicit model that considers the curved input screen and the non-linear projection caused by electromagnetic fields. The CCD camera is modelled according to a general 2D projective transformation of the output screen of the image intensifier. Thus, the back-projection, required for 3D reconstruction, can be expressed in a closed-form. The model is compared to seven other known models. The presented model achieves high accuracy.

Keywords: X-ray imaging system; Calibration; Radioscopy; Computer vision; Image intensifier

1. Introduction

Radioscopy rapidly became the accepted way for controlling the quality of die cast pieces through visual or computer-aided analysis of X-ray images. The purpose of this non-destructive testing method is to identify casting defects, which may be located within the piece and thus are undetectable to the naked eye [1]. The principal aspects of an automated X-ray inspection unit are shown in Fig. 1. Typically, it comprises the following five steps: (i) a manipulator for handling the test piece; (ii) an X-ray source, which irradiates the test piece with a conical beam to generate an X-ray image of the test piece; (iii) an image intensifier which transforms the invisible X-ray image into a visible one; (iv) a CCD camera which records the visible X-ray image, and (v) a computer to process the digital image of the X-ray image and then classify the test piece by accepting or rejecting it.

Flat amorphous silicon detectors can be used as image sensors in some industrial inspection systems. In such detectors, using a semi-conductor, energy from the X-ray is converted directly into an electrical signal (without image intensifier). However, NDT using flat detectors is less feasible due to their higher cost in comparison to image intensifiers. In this paper, we will use the term *radioscopic imaging systems* for imaging systems based on image intensifiers. We concentrate on modelling these systems because they suffer from two significant distortions: geometric and electromagnetic field distortions (EFDs). Additionally, imaging systems based on flat detectors do not suffers from these distortions, and they can be easily modelled with a simple pinhole camera model [2].

The geometric model of the radioscopic imaging system establishes the relationship between 3D coordinates of the object under test and their corresponding 2D digital X-ray image coordinates. The model is required by both reconstructing 3D information from image coordinates and reprojecting 2D image coordinates from 3D information. The 3D reconstruction is the process of determining the 3D position of a point in the object under test, which is identified and matched in at least two different X-ray images of the object. The 3D reconstruction is achieved by the method of *triangulation* that finds the intersection in 3D space of the rays that have produced the image points [2]. This can be performed if we know the *back-projection* of the corresponding image points. 3D reconstruction is performed for example, for inspecting the internal and external geometry of a casting using CAD-models [3]; and for locating features of a 3D object using a stereoscopic technique [4]. An example of inferring 3D and 2D information is given in Ref. [5] where a novel automated

* Tel.: +56-2-776-3511; fax: +56-2-776-5892.
E-mail address: dmery@ieee.org (D. Mery).
[1] www.diinf.usach.cl/~dmery

0963-8695/03/$ - see front matter © 2003 Elsevier Ltd. All rights reserved.
doi:10.1016/S0963-8695(03)00084-7

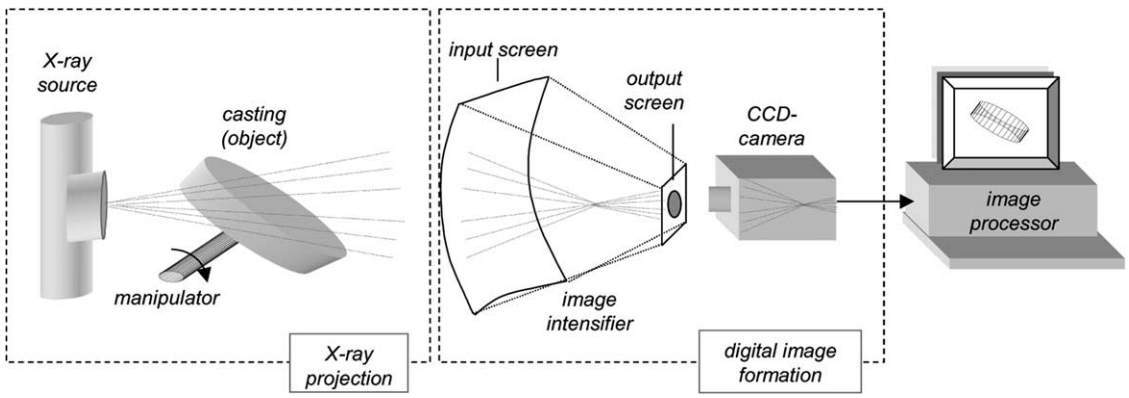

Fig. 1. Diagram of a radioscopic imaging system.

inspection method is presented. In this case the defects are detected by considering the correspondences in multiple views.

The process of determining the parameters involved in the geometric model is called *calibration* [6]. Calibration of imaging systems is a very important issue in computer vision applications that require high accuracy in 3D or 2D measurements. Actual imaging systems are not perfect and show a diversity of deviations. The nominal values of the dimensions of the systems, if they are voluntarily provided by manufacturers, suffer from imprecision. In addition, many parameters of the model cannot be measured or they can be measured only imperfectly. For these reasons, the parameters must be estimated from indirect measurements using a calibration process.

In this paper, we will give a geometric viewpoint about how a radioscopic imaging system can be explicitly modelled. When using explicit models, the physical parameters of the imaging system, like image centre, focal length, etc. are considered independently [7]. The model presented in this paper maps the 3D object into a digital radioscopic image using three transformations as shown in Fig. 1: (i) linear central projection in the X-ray projection; (ii) non-linear transformation in the image intensifier; and (iii) 2D projective transformation in the CCD camera. The goal of our paper is the introduction of a new high accuracy explicit model of the image intensifier, which takes into account the non-linear distortion caused by the curved input screen of the image intensifier (Fig. 1), and the non-linear projection in the image intensifier caused by electromagnetic fields. Using this model, the back-projection function—required for 3D reconstruction—can be calculated in a closed-form.

Finally, we compare the performance of seven existing models with the performance of our explicit model by calibrating a real radioscopic imaging system. The existing models evaluated in our experiments were developed in the last 15 years for calibrating radioscopic systems and cameras, with and without lens distortion.

The paper is organized as follows. Section 2 gives a theoretical background on this topic. The proposed model is described in Section 3. In Section 4, the experiments and results are presented. Finally, Section 5 gives concluding remarks.

2. Theoretical background

2.1. A general model

In this section we present a general model which relates the 3D coordinates of the test object to the 2D coordinates of the digitalised radioscopic image pixel. The model consists of two parts as shown in Fig. 1: X-ray projection and digital image formation. The coordinate systems used in our approach are shown in Fig. 2.

First we will describe how a 3D point M is projected onto a projection plane Π, called the *retinal plane* of the X-ray projection, in which the X-ray image is formed through an operation called *central projection* [8]. In this case, the retinal plane is fictitious and is located tangentially to the input screen of the image intensifier, as shown in Fig. 3. The *optical centre* C of the central projection corresponds to the X-ray source, modelled as a point.[2] The optical centre is located at a distance f, the *focal length* of the retinal plane. The central projection of M onto projection plane Π is the point m. It is defined as the intersection of the line that contains the points C and M with the retinal plane Π. The *optical axis* is defined as the line going through the optical centre C and perpendicular to the retinal plane Π.

We define a 3D *world coordinate system* (WCS) in the optical centre C of the central projection. The coordinates of this coordinate system are $\bar{X}$, $\bar{Y}$, and $\bar{Z}$, where the $\bar{Z}$-axis coincides with the optical axis, as represented in Fig. 3. In WCS, the retinal plane Π is defined by $\bar{Z}=f$. The coordinates of the 3D point M are denoted by $(\bar{X},\bar{Y},\bar{Z})$ in this coordinate system.

[2] Although industrial X-ray generators use standard tubes with larger focal size that blur the X-ray images slightly, the assumption that the X-ray source can be modelled as a point is valid for geometrical measurements. This is because the position of a point in the X-ray image can still be estimated as the centre of the blurred point [9].

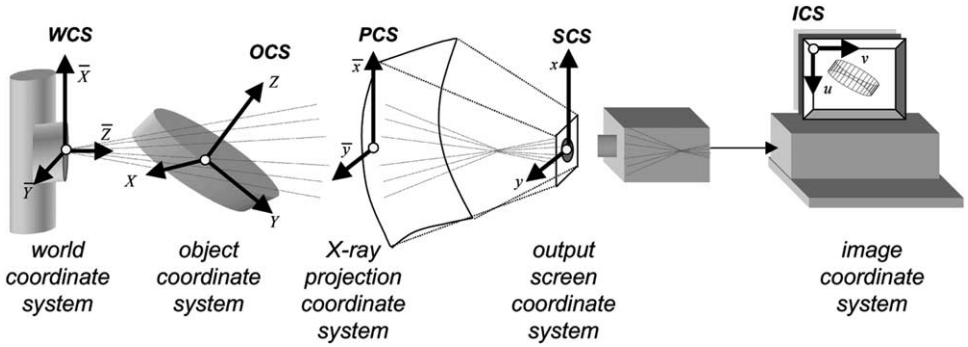

Fig. 2. Diagram of the coordinate systems (see also Fig. 1).

Now, we define a 3D *object coordinate system* (OCS) that is attached to the object to be projected. The coordinates of the 3D point M are denoted by (X, Y, Z) in OCS. The centre of the object is assumed to be at the origin O of this coordinate system, as shown in Fig. 3. The OCS is then considered as a rigid displacement of the WCS represented by a translation 3-component vector $\mathbf{t} = [t_X\ t_Y\ t_Z]^{\mathrm{T}}$ and a 3×3 rotation matrix $\mathbf{R}$. Vector $\mathbf{t}$ represents the origin of OCS given in coordinates of WCS. Matrix $\mathbf{R}$ depends on the Euler angles ω_X, ω_Y and ω_Z (Fig. 3) defined by [6]

$$\mathbf{R} = \mathbf{R}(\omega_X, \omega_Y, \omega_Z) = \begin{bmatrix} R_{11} & R_{12} & R_{13} \\ R_{21} & R_{22} & R_{23} \\ R_{31} & R_{32} & R_{33} \end{bmatrix}, \tag{1}$$

with

$$\begin{aligned} R_{11} &= \cos(\omega_Y)\cos(\omega_Z) \\ R_{12} &= \cos(\omega_Y)\sin(\omega_Z) \\ R_{13} &= -\sin(\omega_Y) \\ R_{21} &= \sin(\omega_X)\sin(\omega_Y)\cos(\omega_Z) - \cos(\omega_X)\sin(\omega_Z) \\ R_{22} &= \sin(\omega_X)\sin(\omega_Y)\sin(\omega_Z) + \cos(\omega_X)\cos(\omega_Z) \\ R_{23} &= \sin(\omega_X)\cos(\omega_Y) \\ R_{31} &= \cos(\omega_X)\sin(\omega_Y)\cos(\omega_Z) + \sin(\omega_X)\sin(\omega_Z) \\ R_{32} &= \cos(\omega_X)\sin(\omega_Y)\sin(\omega_Z) - \sin(\omega_X)\cos(\omega_Z) \\ R_{33} &= \cos(\omega_X)\cos(\omega_Y) \end{aligned}$$

The perspective projection of M onto the projection plane is the 2D point m that is represented as $(\bar{x}, \bar{y})$ in a new 2D coordinate system called the *X-ray projection coordinate system* (PCS). The $\bar{x}$, $\bar{y}$-axes are parallel to the $\bar{X}$, $\bar{Y}$-axes, respectively. Applying Thales theorem, the coordinates of m in this 2D system are $\bar{x} = f\bar{X}/\bar{Z}$ and $\bar{y} = f\bar{Y}/\bar{Z}$. In this approach, *homogeneous coordinates* [2] are used: a point $(a_1, a_2, \ldots, a_N)$ in a N dimensional space is expressed as a homogeneous vector with $N+1$ elements $(b_1, b_2, \ldots, b_N, b_{N+1})$ where $a_i = b_i/b_{N+1}$ for $i = 1, \ldots, N$. In addition, we use the notation of Faugeras [2], where we differentiate between the projective geometric objects themselves and their representations, e.g. a point in the space will be denoted by M whereas its vector in

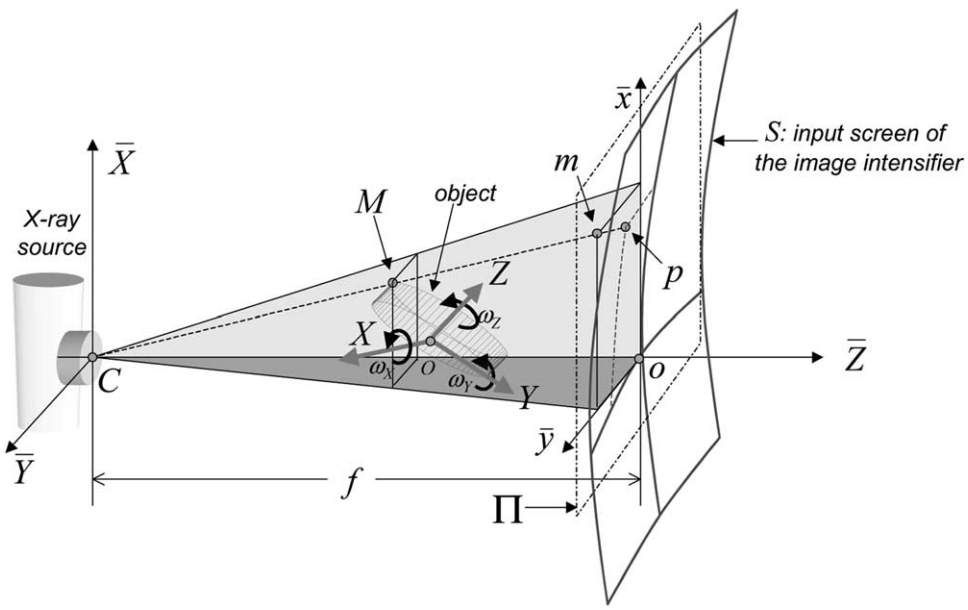

Fig. 3. X-ray projection.

homogeneous coordinates will be denoted by **M**. Thus, the coordinates of point m can be calculated from

$$\begin{bmatrix} \bar{x} \\ \bar{y} \\ 1 \end{bmatrix} \cong \underbrace{\begin{bmatrix} f & 0 & 0 & 0 \\ 0 & f & 0 & 0 \\ 0 & 0 & 1 & 0 \end{bmatrix}}_{\mathbf{E}} \underbrace{\begin{bmatrix} \mathbf{R} & \mathbf{t} \\ \mathbf{0}^{\mathrm{T}} & 1 \end{bmatrix}}_{\mathbf{S}} \begin{bmatrix} X \\ Y \\ Z \\ 1 \end{bmatrix}, \tag{2}$$

where $\mathbf{0}^{\mathrm{T}} = [0\ 0\ 0]$. We use the notation $\cong$ to indicate equality up to multiplication by a scale factor, i.e. $\mathbf{a} \cong \mathbf{b}$ means $\lambda\mathbf{a} = \mathbf{b}$, where λ is a scale factor. Eq. (2) can be rewritten in matrix form as

$$\mathbf{m} \cong \mathbf{PM}, \tag{3}$$

where $\mathbf{P} = \mathbf{ES}$, and the 3-component vector **m** and the 4-component vector **M** are homogeneous representations of $(\bar{x}, \bar{y})$ and (X, Y, Z), respectively (e.g. $\mathbf{m} = [\bar{x}\ \bar{y}\ 1]^{\mathrm{T}}$ and $\mathbf{M} = [X\ Y\ Z\ 1]^{\mathrm{T}}$). Eq. (3) is a linear equation that maps object coordinates to projection plane coordinates. This equation depends on seven parameters:

$$\mathbf{\Theta}_{\mathrm{ext}} = [f\ \omega_X\ \omega_Y\ \omega_Z\ t_X\ t_Y\ t_Z]^{\mathrm{T}}. \tag{4}$$

They are called the *extrinsic* parameters of the X-ray imaging system.

Finally, we introduce the 2D *image coordinate system* (ICS) to represent the pixel coordinates (u, v) of the digital image. The point (u, v) in ICS can be calculated from the point $(\bar{x}, \bar{y})$ in PCS using a function γ

$$\mathbf{w} \cong \gamma(\mathbf{m}), \tag{5}$$

where the 3-component vectors **w** and **m** are homogeneous representations of (u, v) and $(\bar{x}, \bar{y})$, respectively. Several linear and non-linear models of γ, that were developed for radioscopic imaging systems and CCD cameras, will be discussed in Section 2.3. The parameters of γ are called the *intrinsic* parameters. They will be denoted by $\mathbf{\Theta}_{\mathrm{int}}$.

To summarise, using Eq. (3) for the perspective projection and Eq. (5) for the digital image formation, an object point M, whose homogeneous coordinates are $\mathbf{M} = [X\ Y\ Z\ 1]^{\mathrm{T}}$ (in OCS), can be mapped into a 2D point of the digital X-ray image as w, whose homogeneous coordinates are $\mathbf{w} = [u\ v\ 1]^{\mathrm{T}}$ (in ICS) using the following expression

$$\mathbf{w} \cong \gamma(\mathbf{PM}) := \mathbf{F}(\mathbf{\Theta}, \mathbf{M}), \tag{6}$$

where $\mathbf{\Theta} = [\mathbf{\Theta}_{\mathrm{ext}}^{\mathrm{T}}\ \mathbf{\Theta}_{\mathrm{int}}^{\mathrm{T}}]^{\mathrm{T}}$ is the vector of parameters involved in the projection model.

2.2. Calibration

The calibration of an X-ray imaging system—in the context of 3D machine vision—is the process of estimating the parameters of the model, which is used to determine the projection of the 3D object under test into its 2D digital X-ray image. This relationship 3D → 2D can be modelled with the transfer function $\mathbf{F} : \mathscr{R}^3 \rightarrow \mathscr{R}^2$ expressed in Eq. (6).

There are several techniques developed to calibrate an imaging system. They can be roughly classified into two categories: *photogrammetric calibration* and *self-calibration* [10]. The first one is a 3D reference object-based calibration, where the calibration is performed by observing a calibration object whose geometry in 3D space is known with high accuracy [2]. The second technique uses the identification of matching points in several views of a scene taken by the same camera. Self-calibration does not use a calibration object with known 3D geometry because it aims to identify the intrinsic parameters of the imaging system and to reconstruct 3D structure up to a scale similarity [11]. Due to the high precision feature measurement of 3D geometry required in the NDT applications, it would be necessary to do a *true* reconstruction of the 3D space without a scale factor. For this reason, the calibration technique used in our work belongs to the photogrammetric category.

In the calibration, we estimate the parameters of the model based on n points whose object coordinates $\mathbf{M}_i = [X_i\ Y_i \times Z_i\ 1]^{\mathrm{T}}$ are known whose image coordinates $\tilde{\mathbf{w}}_i = [\tilde{u}_i\ \tilde{v}_i\ 1]^{\mathrm{T}}$ are measured, for $i = 1, \ldots, n$. Using Eq. (6) we obtain the *reprojected* points $\mathbf{w}_i = [u_i\ v_i\ 1]^{\mathrm{T}}$, i.e. the inferred projections in the digital image computed from the calibration points $\mathbf{M}_i$ and the parameter vector $\mathbf{\Theta}$. The parameter vector is then estimated by minimising the distance between measured points $(\tilde{\mathbf{w}}_i)$ and inferred points $(\mathbf{w}_i \cong \mathbf{F}(\mathbf{\Theta}, \mathbf{M}_i))$. Thus, the calibration is performed by minimising the objective function $\mu(\mathbf{\Theta})$ defined as the mean-square discrepancy between these points:

$$\mu(\mathbf{\Theta}) = \frac{1}{n} \sum_{i=1}^{n} \|\tilde{\mathbf{w}}_i - \mathbf{w}_i\| \rightarrow \min. \tag{7}$$

The calibration problem is a non-linear optimisation problem. Generally, the minimisation of $\mu(\mathbf{\Theta})$ has no closed-form solution. For this reason, the objective function must be iteratively minimised starting with an initial guess $\mathbf{\Theta}^0$ that can be obtained from nominal values or preliminary reference measurements.

2.3. Geometric model of the imaging system: a review

In this section, we present seven existing models that can be used to calibrate an X-ray imaging system. Five models were conceived to calibrate cameras with and without distortion. The others were developed to calibrate imaging systems with image intensifiers. In all these models, the perspective projection OCS → PCS is done using Eq. (3). For this reason, in this section only the transformation PCS → ICS will be described. We use the definition given in Eq. (5), where a point $\mathbf{m} = [\bar{x}\ \bar{y}\ 1]^{\mathrm{T}}$ in PCS is transformed by a function γ into a point $\mathbf{w} = [u\ v\ 1]^{\mathrm{T}}$ in ICS. Recall that

the parameters of γ are the intrinsic parameters of the imaging system.

Camera models. Faugeras and Toscani present in Ref. [12] a linear model without considering distortion:

$$\begin{bmatrix} u \\ v \\ 1 \end{bmatrix} = \begin{bmatrix} k_u & s & u_0 \\ 0 & k_v & v_0 \\ 0 & 0 & 1 \end{bmatrix} \begin{bmatrix} \bar{x} \\ \bar{y} \\ 1 \end{bmatrix}. \tag{8}$$

The five (intrinsic) parameters of the model consider scale factors (k_u, k_v) in each ordinate, a skew factor (s) that models non-orthogonal u, v-axes, and a translation of the origin (u_0, v_0) that represents the projection of $(\bar{x}, \bar{y}) = (0, 0)$ in ICS. In this linear model, the focal length is normalised to $f = 1$. A linear approach based on a least-squares technique is proposed in Ref. [12] to estimate the intrinsic and extrinsic parameters in a closed-form. However, Faugeras in Ref. [2] proposes minimising the distances between the observations and the model in ICS using the objective function μ of Eq. (7). Faugeras reported that this non-linear method clearly appears to be more robust than the linear method of Faugeras and Toscani when the measured data is perturbed by noise.

In order to model the distortion, a positional error (δ_u, δ_v) can be introduced:

$$\underbrace{\begin{bmatrix} u \\ v \\ 1 \end{bmatrix}}_{\mathbf{w}} = \underbrace{\begin{bmatrix} k_u & 0 & u_0 \\ 0 & k_v & v_0 \\ 0 & 0 & 1 \end{bmatrix} \begin{bmatrix} \bar{x} \\ \bar{y} \\ 1 \end{bmatrix}}_{\mathbf{w}'} + \begin{bmatrix} \delta_u(\bar{x}, \bar{y}) \\ \delta_v(\bar{x}, \bar{y}) \\ 0 \end{bmatrix}. \tag{9}$$

In this model, the ideal non-observable position w' is displaced to the real position w as shown in Fig. 4. The amount of the displacements, δ_u and δ_v, usually depends on the point position $(\bar{x}, \bar{y})$. Several models for the positional error were reported in the literature to calibrate a camera [6,9,13,14]. In these models, the skew s is zero, because in modern digital cameras the u, v-axes can be considered as orthogonal.

The distortion is decomposed into two components: *radial* and *tangential* distortions as shown in Fig. 4. Radial and tangential distortion depend on r and ϕ, respectively, where (r, ϕ) are the polar coordinates of the ideal position $(\bar{x}, \bar{y})$ represented in PCS. Tsai in Ref. [6] uses a simple radial distortion model with only one additional parameter, because his experience with cameras shows that only radial distortion, which is principally caused by flawed radial curvature of the lens elements, needs to be considered.

Weng et al. proposes in Ref. [9] an implicit model that includes radial, decentring and prism distortion. Decentring distortion arises when the optical centres of the lens elements are not exactly collinear, whereas the prism distortion occurs from imperfection in lens design, manufacturing and camera assembly. The last two distortions, modelled with five parameters, have both radial and tangential components.

Heikkilä introduces in Ref. [13] an implicit model for radial and decentring distortion that takes into account an inverse distortion model to express the distorted image coordinates in terms of their undistorted coordinates. The number of parameters of this model is four.

Swaminathan and Nayar present in Ref. [14] a model for wide-angle lenses and polycameras. The model considers a shift of the optical centre, radial distortion and decentring distortion. A shift of the optical centre means a shift of the image detector in the image plane. The suggested total distortion includes four parameters.

Image intensifier models. Two models were reported in the literature to calibrate a radioscopic imaging system composed by image intensifier and CCD camera. The first model was proposed independently by Jaeger in Ref. [15] and Brack et al. in Ref. [16]. They propose an implicit model between PCS and ICS. The transfer function γ is a third degree polynomial with 20 parameters $(a_i, b_i, i = 0, \ldots, 9)$ given by:

$$\begin{bmatrix} u \\ v \end{bmatrix} = \begin{bmatrix} a_0 & \cdots & a_9 \\ b_0 & \cdots & b_9 \end{bmatrix} [1\ \bar{x}\ \bar{y}\ \bar{x}\bar{y}\ \bar{x}^2\ \bar{y}^2\ \bar{y}\bar{x}^2\ \bar{x}\bar{y}^2\ \bar{x}^3\ \bar{y}^3]^{\mathrm{T}}. \tag{10}$$

This cubic function can model not only the distortion caused by the curved input screen, but also the distortion introduced

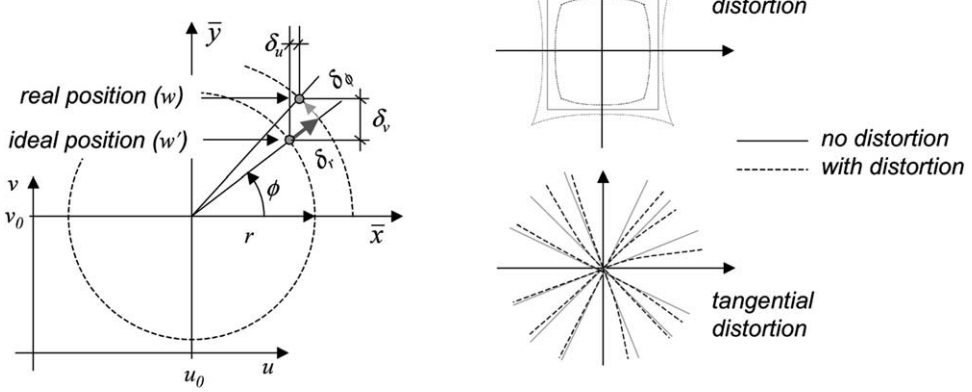

Fig. 4. Radial and tangential distortions [9].

by electromagnetic fields present around the image intensifier.

The second model was developed by Mery and Filbert in Refs. [5,17], in which a hyperbolic surface is used to model the input screen of the image intensifier [18] that is defined by

$$\bar{Z} = S(\bar{X}, \bar{Y}) = f\sqrt{1 + (\bar{X}/a)^2 + (\bar{Y}/b)^2}, \tag{11}$$

with f (the focal length of the X-ray projection) being the real half axis of the hyperboloid; a and b the imaginary half axes. The projection of point M onto the input screen of the image intensifier is denoted by p. It is calculated as the intersection of the line that contains points C, M and m with the 3D surface S (Fig. 3). Its coordinates are given by: $x' = \bar{x}/k(\bar{x},\bar{y})$ and $y' = \bar{y}/k(\bar{x},\bar{y})$, with $k(\bar{x},\bar{y}) = \sqrt{1 - (\bar{x}/a)^2 - (\bar{y}/b)^2}$. The point p is imaged at the CCD camera as w, whose coordinates can be estimated approximately using an affine transformation [2]

$$\begin{bmatrix} u \\ v \\ 1 \end{bmatrix} = \begin{bmatrix} k_u & 0 & u_0 \\ 0 & k_v & v_0 \\ 0 & 0 & 1 \end{bmatrix} \begin{bmatrix} +\cos(\theta) & +\sin(\theta) & 0 \\ -\sin(\theta) & +\cos(\theta) & 0 \\ 0 & 0 & 1 \end{bmatrix} \times \begin{bmatrix} \bar{x}/k(\bar{x},\bar{y}) \\ \bar{y}/k(\bar{x},\bar{y}) \\ 1 \end{bmatrix}, \tag{12}$$

where θ represents rotation between $\bar{x}$, $\bar{y}$- and u, v-axes. This model has only three additional parameters a, b and θ.

3. Proposed model

In this section, we present an explicit model based on the hyperbolic model of Mery and Filbert [5,17] to perform the transformation PCS → ICS that takes place in the image intensifier and CCD camera. The original hyperbolic model, presented in Section 2, does not take into account the non-linear projection between input screen and output screen of the image intensifier, because it is considered as an affine transformation. Additionally, there is no decentring point, since in this model the optical axis of the X-ray projection coincides with the optical axis of the image intensifier. Furthermore, the skew parameter of the CCD camera is not included. Finally, the distortion that arises when electromagnetic fields are present around the image intensifier is not considered. In this section, we propose a complete model that incorporates the mentioned distortion effects.

This section is organized as follows: first, the image intensifier model will be outlined; second the model of the CCD camera will be presented; finally, the solution for the back-projection problem is presented.

3.1. Image intensifier

The image intensifier converts the X-ray image into a bright visual image, that can be captured by a CCD camera [19]. Due to the curvature of the input screen of the image intensifier, the radioscopic image received at the output screen is deformed, especially at the corners of the image. An additional distortion can be caused by electromagnetic fields that perform a non-linear projection. An example of these distortion effects is shown in Fig. 5, where a radioscopic image of a plate containing holes that have been placed in a regular grid manner is illustrated.

First, we will consider a model without electromagnetic field distortion (EFD). The geometry of the model used to compute the distortioned perspective projection is shown in Fig. 6. It consists of a curved input screen S and an output screen Φ, on which the image is projected. The output screen Φ coincides with the retinal plane of this projection. We have shown in Section 2.1, how the 3D object point M is projected onto plane Π as point m. Thus, the perspective X-ray projection OCS → PCS, is given by Eq. (3). In this section we will calculate, how point m is projected onto input screen S as point p and then onto the retinal plane Φ as point r.

The X-ray image present on the input screen is projected onto the output screen through an optical centre of the image intensifier. We may assume without loss of generality that the optical axis of the image intensifier (z-axis) is parallel to the optical axis of the X-ray projection ($\bar{Z}$-axis), because, in a central X-ray projection, there is always a ray that is parallel to the optical axis of the image intensifier. However, the displacement of these axes must be determined. For this reason, we modify the hyperbolic surface of Eq. (11) by introducing a shift of the centre of the hyperboloid as shown in Fig. 6. Therefore, the hyperbolic surface S is defined in WCS by

$$\bar{Z} = S(\bar{X}, \bar{Y}) = f\sqrt{1 + \frac{(\bar{X} - \bar{x}_0)^2}{a^2} + \frac{(\bar{Y} - \bar{y}_0)^2}{b^2}}, \tag{13}$$

with f being the real half axis of the hyperboloid; a and b the imaginary half axes; and $(\bar{x}_0, \bar{y}_0)$ the coordinates of

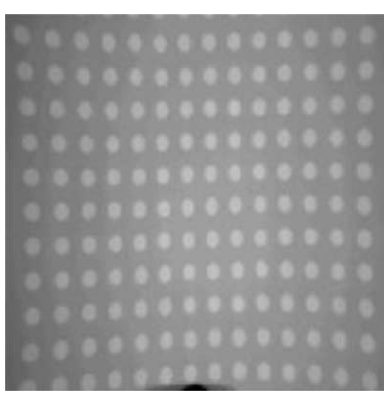

Fig. 5. Radioscopic image of a plate with holes distributed in a regular grid manner.

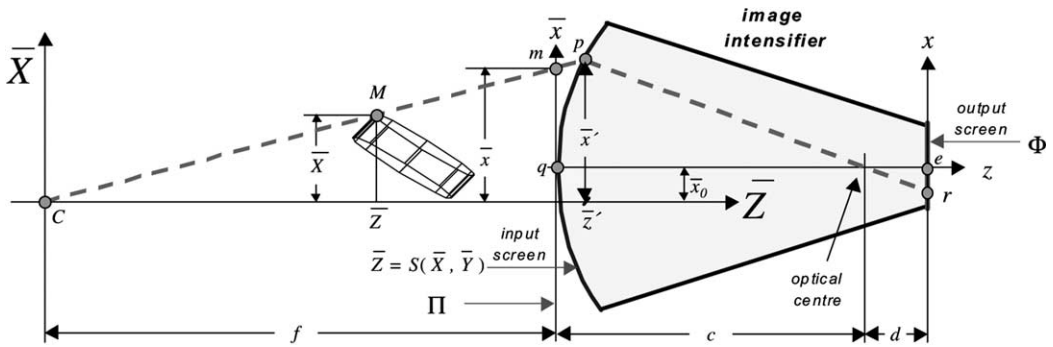

Fig. 6. Geometric model of the image intensifier (axes parallel to $\bar{Y}$ are not shown).

the centre of the hyperboloid. The focal length of the X-ray projection (f), defined in Section 2.1, is the minimal value that takes the surface S. This occurs in $(\bar{x}_0, \bar{y}_0)$, that is represented as q in Fig. 6. The displacement between $\bar{Z}$- and z-axis is given by $(\bar{x}_0, \bar{y}_0)$.

The projection of point M onto the input screen of the image intensifier is calculated as the intersection of the line that contains points C, M and m with the 3D surface S. This intersection is denoted by p in Fig. 6, whose coordinates in WCS are given by $(\bar{x}', \bar{y}', \bar{z}')$

$$\bar{x}' = \bar{z}'\bar{x}/f, \qquad \bar{y}' = \bar{z}'\bar{y}/f \qquad \text{and}$$
$$\bar{z}' = \frac{-B + \sqrt{B^2 - 4AC}}{2A}, \tag{14}$$

with

$$A = \frac{1}{f^2}\left(1 - \frac{\bar{x}^2}{a^2} - \frac{\bar{y}^2}{b^2}\right), \qquad B = \frac{2}{f}\left(\frac{\bar{x}\bar{x}_0}{a^2} + \frac{\bar{y}\bar{y}_0}{b^2}\right),$$
$$C = -\left(1 + \frac{\bar{x}_0^2}{a^2} + \frac{\bar{y}_0^2}{b^2}\right).$$

The coordinates of point p depend on the coordinates $(\bar{x}, \bar{y})$ of point m in PCS. Using homogeneous coordinates, p can be expressed as follows

$$\mathbf{p} = \mathbf{g}(\mathbf{m}), \tag{15}$$

where $\mathbf{p} = [\bar{x}'\ \bar{y}'\ \bar{z}'\ 1]^{\mathrm{T}}$, $\mathbf{m}$ is a homogeneous representation of $(\bar{x}, \bar{y})$, and $\mathbf{g}$ is the non-linear function defined from Eq. (14).

As shown in Fig. 6, point p is projected through the optical centre of the image intensifier onto the output screen Φ as point r. The projected point r has coordinates (x, y) in a new 2D coordinate system, called the *output screen coordinate system* (SCS). This coordinate system is centred in e, and its x, y-axes are parallel to the $\bar{x}, \bar{y}$-axes of PCS. We can conclude from consideration of similar triangles that

$$\begin{bmatrix} x \\ y \\ 1 \end{bmatrix} \cong \begin{bmatrix} d & 0 & 0 & -d\bar{x}_0 \\ 0 & d & 0 & -d\bar{y}_0 \\ 0 & 0 & 1 & -(f+c) \end{bmatrix} \begin{bmatrix} \bar{x}' \\ \bar{y}' \\ \bar{z}' \\ 1 \end{bmatrix}, \tag{16}$$

where c and d are the distances of the input and output screen to the optical centre of the image intensifier (Fig. 6). This equation can be expressed in matrix form as

$$\mathbf{r} \cong \mathbf{D}\mathbf{p}, \tag{17}$$

where the 3-component vector $\mathbf{r}$ is a homogeneous representation of (x, y), and $\mathbf{D}$ is the 3×4 projective matrix of the image intensifier expressed in Eq. (16). From Eqs. (15) and (17) we obtain the non-linear equation, which depends on six parameters: a, b, c, d, $\bar{x}_0$ and $\bar{y}_0$, that maps a projected point on the retinal plane Π of the X-ray projection onto a point on the retinal plane Φ of the image intensifier:

$$\mathbf{r} \cong \mathbf{D}\mathbf{g}(\mathbf{m}). \tag{18}$$

To model the effect of the EFD we propose an empirical model, in which a point r on plane Φ will be transformed into a new point r'. We observed that the projection of a regular grid seems to have an additional harmonic signal (Fig. 5). For this reason, we can empirically model this distortion with sinusoidal functions.

The EFD is modelled in two steps. The first step introduces a distortion in the x direction and the second one in the y direction. Thus, x is firstly transformed into x' from (x, y) and secondly, y is transformed into y' from (x', y) as follows

$$x' = x + A_1 \sin(B_1 y + C_1),$$
$$y' = y + A_2 \sin(B_2 x' + C_2), \tag{19}$$

where A_i, B_i and C_i, $i = 1, 2$, are the parameters of the EFD model. Formally, r' can be expressed using homogeneous

coordinates as follows

$$\mathbf{r}' = \mathbf{f}(\mathbf{r}) = [x' \; y' \; 1]^{\mathrm{T}}, \tag{20}$$

where $\mathbf{f}$ is the non-linear function defined from Eq. (19).

Other sinusoidal functions can be used to model the distortion introduced by electromagnetic fields. The reason why we use a two-step based model is because Eq. (19) can be back-projected in a closed-form as shown in Section 3.3.

3.2. CCD camera

The 2D *image coordinate system* (ICS) is used to represent the pixel coordinates of the radioscopic image captured by the CCD camera. The point r (or r' if we consider the EFD) at the output screen of the image intensifier (Fig. 6) is projected onto the plane Γ of the CCD-array as point w as shown in Fig. 7.

The camera could be modelled as a general pinhole camera [2], in which a projective mapping from a 3D point of the space to a 2D projective space takes place. However, in our model the 3D points to be mapped belong to a plane, namely the plane Φ. For this reason, in this work we use a 2D → 2D general projective transformation called *homography* [8] which relates the coordinates of plane Φ to retinal plane Γ of the camera. This transformation is defined by

$$\mathbf{w} \cong \mathbf{H}\mathbf{r}, \tag{21}$$

where the 3-component vectors $\mathbf{r}$ and $\mathbf{w}$ are homogeneous representations of (x, y) and (u, v) (coordinates of r in SCS and w in ICS), respectively. Matrix $\mathbf{H}$ is a homogeneous 3×3 matrix that causes a general perspective transformation where rotation, translation, scaling, skew and perspective distortion are considered. Matrix $\mathbf{H}$ has nine elements where only their ratio is significant, so the transformation is defined by only eight parameters, e.g. $h_{11}, h_{12}, \ldots, h_{32}$. Parameter h_{33} can be defined as $h_{33} = 1$.

3.3. Back-projection

The 3D reconstruction is the process of determining the 3D position of a point in the object under test, which is identified and matched in at least two different X-ray views of the object. The 3D reconstruction is achieved by the method of triangulation that finds the intersection in OCS of the rays that have produced the image points. This can be performed if we know the corresponding image points in PCS, i.e. if the image points (u, v) are *back-projected* into the retinal plane Π as $(\bar{x}, \bar{y})$. Having $(\bar{x}, \bar{y})$ the corresponding 3D point can be reconstructed using for example a least-square technique [2]. In this section we present how a point w, whose coordinates in ICS are (u, v), can be back-projected into a point m, whose coordinates in PCS are $(\bar{x}, \bar{y})$. The back-projection is done in two steps: transformation ICS → SCS and transformation SCS → PCS.

Transformation ICS → SCS. Without considering the EFD, the transformation ICS → SCS can be directly obtained from (Eq. (21)):

$$\mathbf{r} \cong \mathbf{H}^{-1}\mathbf{w}. \tag{22}$$

However, if the EFD is considered, the inverse function of Eq. (20) $\mathbf{r} = \mathbf{f}^{-1}(\mathbf{r}')$ must be obtained from Eq. (19):

$$\begin{aligned} y &= y' - A_2 \sin(B_2 x' + C_2), \\ x &= x' - A_1 \sin(B_1 y + C_1). \end{aligned} \tag{23}$$

Therefore, it yields

$$\mathbf{r} = \mathbf{f}^{-1}(\mathbf{H}^{-1}\mathbf{w}). \tag{24}$$

Transformation SCS → PCS. The second transformation is non-linear because it takes into account the geometric distortion of the image intensifier. Given the coordinates (x, y) of point r in SCS, a point p on the surface S (Fig. 6) that is the back-projection of r can be computed by finding the coordinates $(\bar{x}', \bar{y}', \bar{z}')$ that satisfy Eqs. (13) and (16)

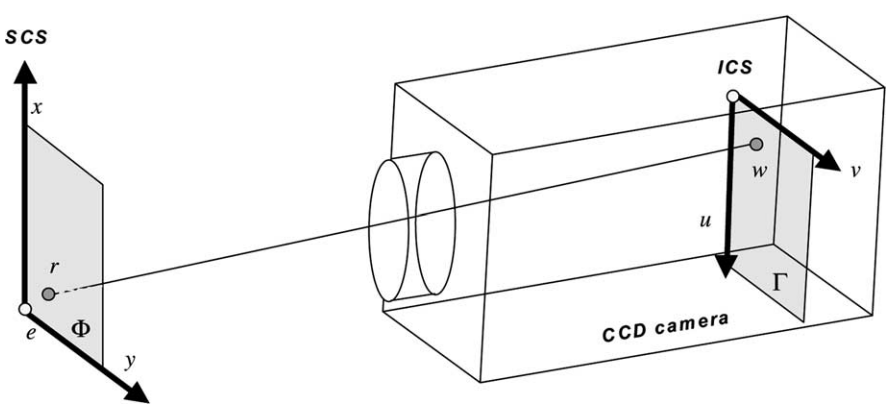

Fig. 7. Imaging process in the CCD camera.

simultaneously. The solution is

$$\bar{x}' = \bar{x}_0 - \frac{x}{d}(f + c - \bar{z}'), \qquad \bar{y}' = \bar{y}_0 - \frac{y}{d}(f + c - \bar{z}'),$$
$$\bar{z}' = \frac{-B' + \sqrt{B'^2 - 4A'C'}}{2A'}, \tag{25}$$

where

$$A' = \frac{g}{f^2} - 1, \qquad B' = 2(f + c), \qquad C' = -g - (f + c)^2,$$

$$g = \frac{d^2}{\frac{x^2}{a^2} + \frac{y^2}{b^2}},$$

or using matrix notation

$$\mathbf{p} = \mathbf{h}(\mathbf{r}), \tag{26}$$

where $\mathbf{p} = [\bar{x}'\ \bar{y}'\ \bar{z}'\ 1]^{\mathrm{T}}$, $\mathbf{r}$ is a homogeneous representation of (x, y), and $\mathbf{h}$ is the non-linear function defined from Eq. (25).

Now, the coordinates of the back-projected point m on the projection plane can be calculated from Eq. (25) and the first two equations of Eq. (14):

$$\bar{x} = f\bar{x}'/\bar{z}' \qquad \textit{and} \qquad \bar{y} = f\bar{y}'/\bar{z}'. \tag{27}$$

Eqs. (22), (26) and (27) can be joined in

$$\mathbf{m} \cong \mathbf{Eh}(\mathbf{H}^{-1}\mathbf{w}), \tag{28}$$

where $\mathbf{E}$ is the 3×4 perspective projection matrix expressed in Eq. (2). However, if the EFD is taken into account, the homogeneous representation of m is from Eq. (24):

$$\mathbf{m} \cong \mathbf{Eh}(\mathbf{f}^{-1}(\mathbf{H}^{-1}\mathbf{w})). \tag{29}$$

3.4. Summary

In Section 3, we propose a model which relates the transformation 3D → 2D, from a 3D point M of the test object to a 2D point w of the digitalised radioscopic image pixel using homogeneous coordinates. Therefore, the transformation is expressed by $\mathbf{M} \rightarrow \mathbf{w}$, where $\mathbf{M} = [X\ Y\ Z\ 1]^{\mathrm{T}}$ and $\mathbf{w} = [u\ v\ 1\ ]^{\mathrm{T}}$. There are two possibilities for performing the transformation, namely without and with considering the EFD. In the first case, the transformation is given by: $\mathbf{M} \rightarrow \mathbf{m} \rightarrow \mathbf{r} \rightarrow \mathbf{w}$ using Eqs. (3), (18) and (21), respectively, i.e.

$$\mathbf{w} \cong \mathbf{HDg}(\mathbf{PM}). \tag{30}$$

This model has seven intrinsic parameters (defined in Eq. (4)) and 14 intrinsic parameters: $a, b, c, d, \bar{x}_0, \bar{y}_0, h_{11}, h_{12}, \ldots, h_{31}$ and h_{32}.

In the second case, where the EFD is modelled, the transformation is expressed by: $\mathbf{M} \rightarrow \mathbf{m} \rightarrow \mathbf{r} \rightarrow \mathbf{r}' \rightarrow \mathbf{w}$ using Eqs. (3), (18), (20) and (21), respectively, i.e.

$$\mathbf{w} \cong \mathbf{HDf}(\mathbf{g}(\mathbf{PM})). \tag{31}$$

In comparison with the first case model, the consideration of the EFD requires six more intrinsic parameters: A_i, B_i and C_i, for $i = 1, 2$.

Finally in Section 3.3, we give the equations for the back-projection $\mathbf{w} \rightarrow \mathbf{m}$ in a closed-form. The equation are expressed in Eqs. (28) and (29) for the cases without and with EFD, respectively.

4. Experiments and results

In this section, we present the experiments which we did in order to evaluate the performance of the models, and their corresponding results obtained by calibrating a real radioscopic imaging system. The tested models and their principal features are summarised in Table 1. They are the seven models outlined in Section 2.3 and the two proposed models of Section 3 (without and with considering EFD). In the presentation of the results, each model will be identified by the name given in the second column of Table 1.

As explained in Section 2.2, the calibration process estimates the parameters of a model based on points whose object coordinates are known, and whose image coordinates are measured. The calibration object used in our experiments is shown in Fig. 8(a). It is an aluminium object with an external diameter of 70 mm. A CAD-model was developed by measurement of the calibration object (Fig. 8(b)). It has 70 small holes ($\phi = 3$–5 mm) distributed on four rings and the centre. As shown in Fig. 8, the centres of gravity of the holes are arranged in three heights.

The search for the calibration points within the X-ray image is done with a simple procedure that detects regions with high contrast and defined size for the area. The centres of gravity of the detected regions, computed with a subpixel accuracy, are defined to be the calibration points. Only complete enclosed regions will be segmented. Fig. 8(c) shows an example of the search for the calibration points within a X-ray image. The correspondence between the 3D object points and their images was established manually. The image intensifier used in the experiments was the XRS 232[3] with 22 cm input screen. The size of the images was 576×768 pixels.

In our experiments, the calibration object was placed in different positions using the MU2000[3] manipulator. The positions of the calibration object were achieved by rotating one of the axes of the manipulator. Some of the images obtained are shown in Fig. 9. In order to incorporate the movement of the manipulator into the geometric model, we

[3] Developed by YXLON International Inc. [20].

Table 1
Characterisation of the implemented models

Model	Name	Reference	Year	Intrinsic parameters	Back-projection	Calibration	Distortion	Model
1. Faugeras	`Linear`	[2]	1993	5	Direct	Iterative	None	Explicit
2. Tsai	`Radial`	[6]	1987	5	Indirect	Iterative	Radial	Implicit
3. Weng et al.	`Rad-Tan-1`	[9]	1992	9	Indirect	Iterative	Radial, tangential	Implicit
4. Heilikkä	`Rad-Tan-2`	[13]	2000	8	Direct	Iterative	Radial, tangential	Implicit
5. Swaminathan and Nayar	`Rad-Tan-3`	[14]	2000	8	Indirect	Iterative	Radial, tangential	Implicit
6. Jaeger, Brack et al.	`Cubic`	[15,16]	1990, 1996	20	Indirect	Iterative	Cubic	Implicit
7. Mery and Filber	`Hyp-Simple`	[5,17]	2000	7	Direct	Iterative	Hyperbolic simple	Explicit
8. Proposed 1 without EFD	`Hyp-Full`	Sections 3.1 and 3.2	2003	14	Direct	Iterative	Hyperbolic	Explicit
9. Proposed 2 with EFD	`Hyp-EFD`	Sections 3.1 and 3.2	2003	20	Direct	Iterative	Hyperbolic, sinusoidal	Explicit

modify Eq. (2) by:

$$\begin{bmatrix} \bar{x} \\ \bar{y} \\ 1 \end{bmatrix} \cong \underbrace{\begin{bmatrix} f & 0 & 0 & 0 \\ 0 & f & 0 & 0 \\ 0 & 0 & 1 & 0 \end{bmatrix}}_{\mathbf{E}} \underbrace{\begin{bmatrix} \bar{\mathbf{R}} & \bar{\mathbf{t}} \\ \mathbf{0}^{\mathrm{T}} & 1 \end{bmatrix}}_{\bar{\mathbf{S}}} \underbrace{\begin{bmatrix} \mathbf{R} & \mathbf{t} \\ \mathbf{0}^{\mathrm{T}} & 1 \end{bmatrix}}_{\mathbf{S}} \begin{bmatrix} X \\ Y \\ Z \\ 1 \end{bmatrix}. \tag{32}$$

In this equation, we have two 4×4 matrices ($\mathbf{S}$ and $\bar{\mathbf{S}}$) that define, respectively, two 3D Euclidean transformations: (i) between object and manipulator coordinate systems, and (ii) between manipulator and WCSs. The translation vectors ($\mathbf{t}$ and $\bar{\mathbf{t}}$) and the rotation matrices ($\mathbf{R}$ and $\bar{\mathbf{R}}$) are related to the corresponding translation and rotation of the mentioned transformations. Since the calibration object is fixed to manipulator, matrix $\mathbf{S}$ is constant for each position: $\mathbf{t} = [t_X\ t_Y\ t_Z]^{\mathrm{T}}$ and a matrix $\mathbf{R}$ is calculated from the Euler angles ω_X, ω_Y and ω_Z. However, matrix $\bar{\mathbf{S}}$ depends on the position of the manipulator respect to the WCS. Matrix $\bar{\mathbf{S}}$ is defined by a translation vector $\bar{\mathbf{t}} = [\bar{t}_X\ \bar{t}_Y\ \bar{t}_Z]^{\mathrm{T}}$ and a rotation matrix $\bar{\mathbf{R}}$ computed from the Euler angles $\bar{\omega}_X$, $\bar{\omega}_Y$ and $\bar{\omega}_Z$. In our experiments, $\bar{t}_X$, $\bar{t}_Y$, $\bar{t}_Z$, $\bar{\omega}_X$ and $\bar{\omega}_Y$ were constant. Nevertheless, $\bar{\omega}_Z$ was incremented by the manipulator in constant steps. Thus, the rotation of this axis can be linearly modelled by $\bar{\omega}_Z(k) = \bar{\omega}_{Z0} + k\Delta\bar{\omega}_Z$, where k denotes the number of the position. This new model introduces seven additional extrinsic parameters ($\bar{t}_X$, $\bar{t}_Y$, $\bar{t}_Z$, $\bar{\omega}_X$, $\bar{\omega}_Y$, $\bar{\omega}_{Z0}$ and $\Delta\bar{\omega}_Z$) that must be estimated in the calibration process as well.

The calibration is performed by minimising the mean reprojection error (μ) computed as the average of

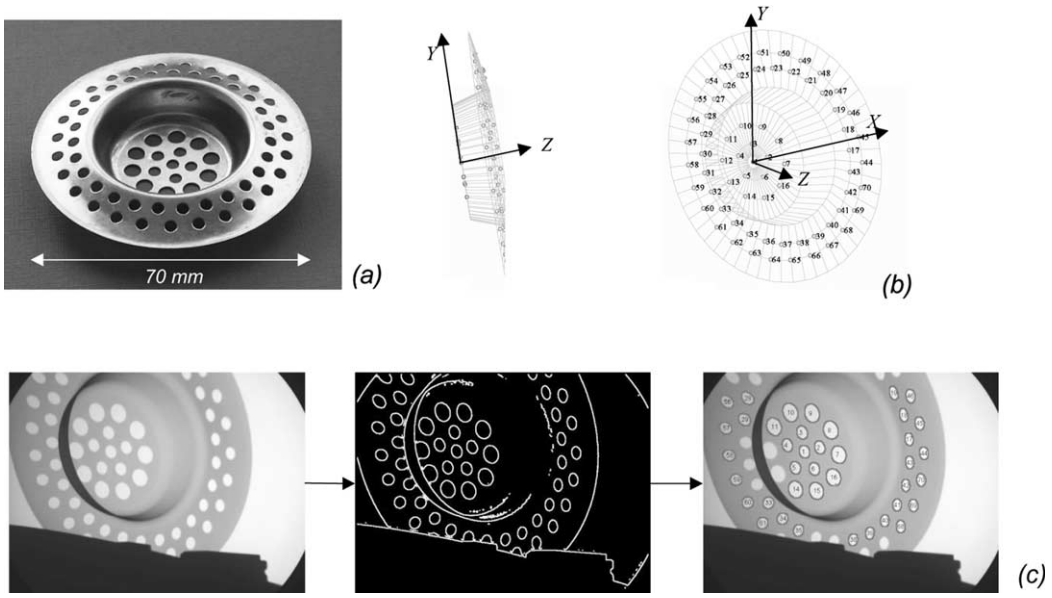

Fig. 8. Calibration object: (a) photography; (b) CAD-model; and (c) radioscopic image of the calibration object and calibration points.

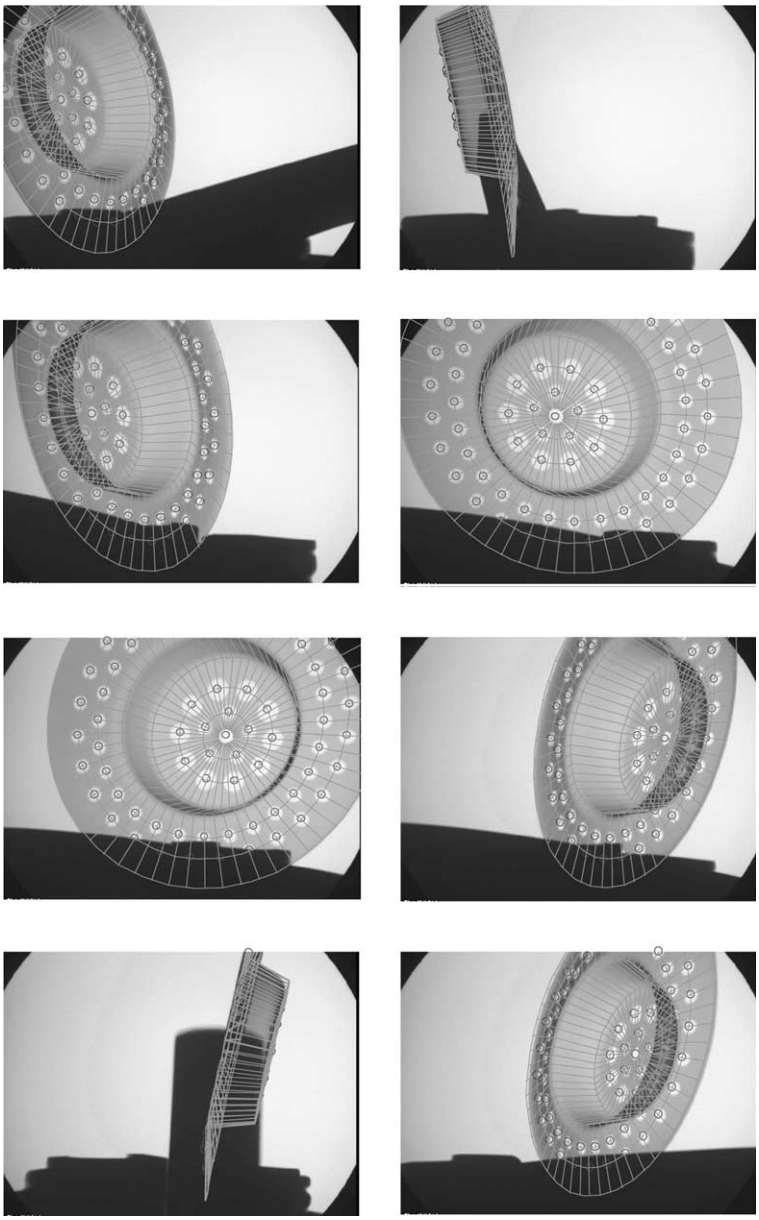

Fig. 9. Calibration results using the proposed method `Hyp-EFD`.

the distance between measured points ($\tilde{\mathbf{w}}_{ik}$) and inferred points ($\mathbf{w}_{ik}$)—in the ICS—obtained from the kth projection of the ith object point $\mathbf{M}_i$ according to the model of the imaging system. As explained in Section 2.2, the calibration problem is a non-linear optimisation problem, where the minimisation of the objective function has no closed-form solution. For this reason, the objective function must be iteratively minimised starting with an initial estimated value for the parameters involved in the model. In our experiments, the estimation is achieved using the well known algorithm for minimisation problems: the *BFGS Quasi-Newton* method,[4] which is implemented by MathWorks Inc. in the optimisation toolbox of MATLAB [21].

We subdivided the calibration points into two groups: the points measured from seven images ($k = 1, 3, 5, \ldots, 13$), were used as *control points* to calibrate the imaging system, whereas the points extracted from seven other images ($k = 2, 4, 6, \ldots, 14$) were used as *test points* in order to evaluate the accuracy of calibration.

An example of the calibration using our proposed model `Hyp-EFD` is shown in Fig. 9. We can see that the modelled projection of a CAD-model of the calibration object coincides with the radioscopic image very well. Although points of the top right and the bottom left images of Fig. 9 could not be used as control (or test) points because they are

[4] This is a gradient method that uses the Broyden–Fletcher–Goldfarb–Shanno formula for updating the approximation of the Hessian matrix iteratively, which reduces the computational cost of the minimisation.

Table 2
Error of the models in control (C) and test (T) points

Model ↓	2D reprojection (pixels)				3D reconstruction (mm)			
	μ		σ		μ		σ	
	C	T	C	T	C	T	C	T
1. `Linear`	2.52	2.45	1.57	1.53	0.47	0.41	0.229	0.157
2. `Radial`	1.70	1.64	0.96	0.83	0.18	0.17	0.087	0.075
3. `Rad-Tan-1`	1.40	1.39	0.85	0.76	0.15	0.15	0.076	0.071
4. `Rad-Tan-2`	1.62	1.66	0.87	0.87	0.25	0.21	0.123	0.092
5. `Rad-Tan-3`	1.64	1.62	0.92	0.81	0.20	0.18	0.102	0.079
6. `Cubic`	1.16	1.16	0.67	0.59	0.15	0.14	0.079	0.063
7. `Hyp-Simple`	1.36	1.40	0.77	0.73	0.18	0.17	0.090	0.074
8. `Hyp-Full`	1.25	1.29	0.72	0.69	0.17	0.16	0.096	0.072
9. `Hyp-EFD`	1.18	1.17	0.71	0.64	0.16	0.14	0.084	0.069

very intricate, the inferred projection of the CAD-model in these positions seems to be fine.

In order to asses the performance of each model, we carried out two experiments: 2D reprojection and 3D reconstruction. The results are summarised in Table 2. The first experiment estimates the parameters of each model by minimising the average error of the reprojection error—in ICS given in pixels—of the control points. The accuracy is assessed with the reprojection error in the test points. Once the calibration is done, the second experiment is performed using the parameters estimated in the first. The 3D reconstruction of the measured points was performed using a least square technique [2]. As a performance measurement of the second experiment, the Euclidean distance between measured and reconstructed points in OCS was calculated in millimetres. The mean μ and the standard deviation σ of the computed distances errors in control and test points were tabulated for each experiment. For emphasis, we remind the reader that the calibration is performed by minimising the average of the reprojection error of the control points (first column in Table 2), i.e. the control points in the experiments of 3D reconstruction were not used to calibrate, but also as test points too.

Since the results obtained on control and test points are very similar, our analysis will consider test point measurements only. The two values x/y given below correspond to the mean error values obtained by computing the 2D reprojection and 3D reconstruction given in pixels and millimetres, respectively. We observe that the best results were obtained by `Cubic` and `Hyp-EFD` models in both experiments. In these cases the mean errors were on the order of 1.16–1.17/0.14, i.e. 1.16–1.17 pixels for the 2D reprojection, and 0.14 mm for the 3D reconstruction. Although `Cubic` model obtains a little bit better accuracy than model `Hyp-EFD` (see standard deviations), we must take into account that `Cubic` model uses an implicit model with 20 parameters for the projection, and 20 other parameters for the back-projection. On the other hand, model `Hyp-EFD` uses the same 20 parameters for both projection and back-projection.

In our experiments, the radioscopic imaging system could not be adequately modelled without consideration of the lens distortion or with only radial and tangential distortion. The models that were originally developed for cameras (`Linear`, `Radial`, `Rad-Tan-1`, `Rad-Tan-2` and `Rad-Tan-3`, where the mean errors were 2.45/0.41, 1.64/0.17, 1.39/0.15, 1.66/0.21 and 1.62/0.18, respectively), did not work appropriately for our radioscopic imaging system. In many cases, the maximum reprojection error was greater than 4 pixels. The reason for this is that the distortion introduced by the image intensifiers is different than the distortion introduced by a camera lens and the camera models do not consider the EFD in the image intensifier.

On the other hand, hyperbolic models are used by `Hyp-Simple`, `Hyp-Full` and `Hyp-EFD`. The results obtained with model `Hyp-Simple` are comparable with the best results obtained from camera models (`Rad-Tan-1`), where the mean errors were 1.40/0.17 and 1.39/0.15, respectively. In relation to model `Hyp-Simple`, model `Hyp-Full` introduces a decentring point and a non-linear transformation in the image intensifier. This additional complexity in the model has a significant decrease in the reprojection error (1.40/0.17 vs. 1.29/0.16). In addition, another important reduction of both errors is achieved by considering the EFD in model `Hyp-EFD` (1.29/0.16 vs. 1.17/0.14).

5. Concluding remarks

In this paper a new high accuracy model of a radioscopic imaging system was presented. The proposed explicit model considers the physical parameters of the imaging system, like image centre, focal length, etc. independently. The model is able to map the 3D coordinates of a test object to the 2D coordinates of the corresponding pixel on the digital radioscopic image. The model consists of three parts: X-ray projection, image intensifier and CCD camera. The distortion introduced by the image intensifier was modelled using a hyperbolic surface for the input screen and sinusoidal functions for electromagnetic fields. Using our explicit model, the back-projection function—required for 3D reconstruction—can be calculated directly using a closed-form solution.

The suggested model was experimentally compared with seven other models, which are normally used to calibrate an imaging system with and without lens distortion. Fourteen radioscopic images were taken of a calibration object in different positions. Seven of them were used to calibrate the imaging system and the other seven were employed to test the accuracy of calibration. The results show that the consideration of only radial and tangential distortions is not good enough if we are working with image intensifiers. In this case, other models must be used for high accuracy

requirements. For this reason, `Cubic` or `Hyp-EFD` models are recommended. Their mean errors are very similar as shown in Table 2. However, for the back-projection, it is convenient to use the proposed model `Hyp-EFD` because the same parameters are used for both the projection and the back-projection model.

Acknowledgements

The author would like to thank the Department for Research and Development of the Unuersidad de Santiago de Chile (project DICYT 06-0119MQ) for financing this investigation.

References

[1] Mery D, Filbert D, Jaeger Th. Image processing for fault detection in aluminum castings. In: MacKenzie DS, Totten G, editors. Analytical characterization of aluminum and its alloys. New York: Marcel Dekker; 2003. in press.
[2] Faugeras O. Three-dimensional computer vision: a geometric viewpoint. Cambridge, MA, London: MIT Press; 1993.
[3] Noble A, Gupta R, Mundy J, Schmitz A, Hartley R. High precision X-ray stereo for automated 3D CAD-based inspection. IEEE Trans Robotics Autom 1998;14(2):292–302.
[4] Evans JP, Robinson M, Godber SX. A new stereoscopic X-ray imaging technique using a single X-ray source: theoretical analysis. NDT&E Int 1996;29(1):27–35.
[5] Mery D, Filbert D. Automated flaw detection in aluminum castings based on the tracking of potential defects in a radioscopic image sequence. IEEE Trans Robotics Autom December 2002;18(6):890–901.
[6] Tsai R. A versatile camera calibration technique for high-accuracy 3D machine vision metrology using off-the-shelf TV cameras and lenses. IEEE Trans Robotics Autom 1987;RA-3(4):323–44.
[7] Wei G-Q, Ma SD. Implicit and explicit camera calibration: theory and experiments. IEEE Trans Pattern Anal Machine Intell 1994;16(5):469–80.
[8] Hartley RI, Zisserman A. Multiple view geometry in computer vision. Cambridge: Cambridge University Press; 2000.
[9] Weng J, Cohen P, Herniou M. Camera calibration with distorsion models and accuracy evaluation. IEEE Trans Pattern Anal Machine Intell 1992;4(10):965–80.
[10] Zhang Z. A flexible new technique for camera calibration. IEEE Trans Pattern Anal Machine Intell 2000;22(11):1330–4.
[11] Luong Q-T, Faugeras O. Self calibration of a moving camera from point correspondences and fundamental matrices. Int J Comput Vis 1997;22(3):261–89.
[12] Faugeras O, Toscani G. The calibration problem for stereo. In Proceedings IEEE Computer Vision and Pattern Recognition 1986;15–20.
[13] Heikkilä J. Geometric camera calibration using circular control points. IEEE Trans Pattern Anal Machine Intell 2000;22(10):1066–77.
[14] Swaminathan R, Nayar SK. Nonmetric calibration of wide-angle lenses and polycameras. IEEE Trans Pattern Anal Machine Inell 2000;22(10):1172–8.
[15] Jaeger Th. Methods for rectification of geometric distortion in radioscopic images. Master theses, Institute for Measurement and Automation, Faculty of Electrical Engineering, Technical University of Berlin, 1990 (in German).
[16] Brack Ch, Götte H, Gossé F, Moctezuma J, Roth M, Schweikard A. Towards accurate X-ray camera calibration in computer-assisted robotic surgery. In Proceedings of International Symposium on Computer Assisted Radiology (CAR), Paris 1996;721–8.
[17] Mery D, Filbert D. The epipolar geometry in the radioscopy: theory and application. at—Automatisierungstechnik 2000;48(12):588–96. in German.
[18] Felix R, Ramm B. Das Röntgenbild, 3rd ed. Stuttgart, New York: Georg Thieme Verlag; 1988.
[19] Halmshaw R. Non-destructive-testing, 2nd ed. London: Edward Arnold; 1991.
[20] YXLON International Inc., Hamburg. *MU2000: 160kV X-ray System, technical data*, 1998. Available: http://www.yxlon.com/mu2000.htm.
[21] MathWorks Inc. *Optimization Toolbox for Use with MATLAB: User's Guide*. The MathWorks Inc., September 2000.